International Journal of Multiphase Flow 203 (2026) 105873

Contents lists available at ScienceDirect

International Journal of Multiphase Flow

journal homepage: www.elsevier.com/locate/ijmulflow

Research Paper

Spatially resolved gas fraction measurements in a bubble column through three-angled X-ray tomography

Rik Volger [a],*, Sam J. den Hartog [a], Evert C. Wagner [b], Cees Haringa [a]

[a] Delft University of Technology, Faculty of Applied Sciences, Department of Biotechnology, Van der Maasweg 9, 2629 HZ, Delft, The Netherlands
[b] Delft University of Technology, Faculty of Applied Sciences, Department of Chemical Engineering, Van der Maasweg 9, 2629 HZ, Delft, The Netherlands

ARTICLE INFO

Dataset link: https://doi.org/10.4121/29b1c43a-7c80-4fc4-a651-6e0e710b77ae

Keywords:
Gas-liquid flows
X-ray tomography
Bubble column
Gas fraction measurement
Fiber probe

ABSTRACT

Bubble columns are a popular choice for large-scale bioprocesses, yet model-based performance predictions provide major uncertainties in scale-up. High-resolution experimental data on local gas fraction and bubble size distribution are essential for reducing these uncertainties. Unfortunately, experimental characterization of gas-phase dynamics is often challenging. This study investigates a 3-angled X-ray tomography setup for measurement of spatially resolved gas fraction profiles in a 20 cm internal diameter bubble column with 100 cm static liquid height. X-ray scatter and beam hardening are identified as main sources of measurement error, and corrections were proposed and tested.

It was found that software-based post-processing image corrections could correct for the effects of both beam hardening and cross-scatter resulting in gas fraction profiles that closely matched literature data for superficial gas velocity ($u_{g,s}$) of 1.7 cm s^{-1}, 4.6 cm s^{-1}, 5.8 cm s^{-1} and 8.6 cm s^{-1}. Comparison between X-ray tomography and radial profiles from optical fiber probe and pressure probe measurements showed a discrepancy, with the fiber probe and pressure probes reporting roughly 20 % lower gas fraction values. An extra correction term might be needed to bring X-ray tomography into quantitative agreement with the complementary measurement methods.

Overall, our work shows that three-angled X-ray tomography allows for rapid and reliable acquisition of gas fraction profiles in scale-invariant bubble columns. The method is a factor twelve faster than optical fiber probes, with increased radial resolution, but lacking the spatial and temporal resolution to identify single bubbles. The combination of X-ray tomography for gas fraction and fiber probes for bubble size distribution is an attractive setup for systematic studies gas phase dynamics in bubble columns.

1. Introduction

Bubble columns are widely used in large-scale bioprocesses due to their simple design and low operating costs, making them attractive for products with narrow profit margins such as bulk chemicals or food proteins. The performance of bubble columns is primarily governed by gas-phase behavior, which dictates mass transfer and mixing efficiency. The presence of dissolved compounds can significantly alter gas-phase dynamics (Volger et al., 2024; Puiman et al., 2022a), a phenomenon that unfortunately remains poorly understood and badly captured in predictive models (Puiman et al., 2022b).

Predictive modeling of bubble column hydrodynamics spans a wide range of approaches, from simplified zero-dimensional models to one-dimensional frameworks and full-fidelity computational fluid dynamics (CFD). These methods have been extensively validated for air–water systems (Sanyal et al., 1999; Mcclure et al., 2014; Draw and Rzehak, 2024), yet incorporating the effects of dissolved compounds remains a major challenge (Puiman et al., 2022b). Some models broadly classify systems as either coalescent or non-coalescent (Chisti and Moo-Young, 1987; van 't Riet, 1983) while others try and capture the continuous response to single solutes or solute groups (Nedeltchev et al., 2024; Helchi et al., 2024; Wang et al., 2024). Few models capture the effects of mixed solutes and even experimental data is lacking. Bioprocesses work with complex mixtures, which results in design uncertainties of 20 % to 40 % (Puiman et al., 2022b). For processes with small margins, such uncertainties can make the difference between making a profit or running at a loss.

* Corresponding author.
E-mail addresses: rvolger@gmail.com (R. Volger), sjdenhartog@tudelft.nl (S.J.d. Hartog), e.c.wagner@tudelft.nl (E.C. Wagner), c.haringa@tudelft.nl (C. Haringa).

https://doi.org/10.1016/j.ijmultiphaseflow.2026.105873
Received 13 February 2026; Received in revised form 26 June 2026; Accepted 30 July 2026
Available online 10 August 2026

High-resolution experimental data on local gas fraction and bubble size distribution (BSD) are essential for improving these models, particularly for validating correction factors in advanced CFD simulations. Such experimental insights can bridge the gap between simplified assumptions and the complex reality of industrial bubble columns.

Unfortunately, experimental characterization of gas-phase dynamics at appreciable gas flow rates and gas holdup (>5 %) is challenging in clear fluids (Poelma, 2020; Villafañe et al., 2025). In fermentation broths, due to the opacity of the liquid, these problems are omnipresent. Global gas holdup can be accurately measured with pressure probes, or less accurately with the liquid bed expansion technique. For spatially resolved holdup measurements far fewer methods are available, especially in large columns that exhibit scale-invariant hydrodynamics. The minimum size required for this is defined by a minimal inner diameter (ID) and ratio of ungassed liquid height (H_L) to ID (ID > 15 cm and H_L/ID > 5) assuming an aqueous mixture (Wilkinson et al., 1992; Besagni and Inzoli, 2016). An often-employed method is the use of optical fiber probe (FP), which can provide a coarse radial profile of both gas fraction and BSD (Augier and Raimundo, 2021; Besagni, 2021; Schweitzer et al., 2001; Esmaeili et al., 2015). Due to time constraints, radial resolution for fiber probe measurements is usually limited to a maximum of 10 positions or 1 cm to 2 cm between measurement points. For each of these positions, measurement duration should span over multiple column oscillations, resulting in measurement times of 60 s to 120 s per position (Becker et al., 1999). Similar constraints hold for other invasive point probes such as conductivity probes. When these constraints are overcome, for example by using wire-mesh sensors, the result is a strong impact on the flow patterns in the column (Prasser et al., 2001). X-ray and γ-ray tomography provide non-invasive and high resolution alternatives for resolving radial gas distribution profiles without requiring a transparent fluid (Heindel, 2011; Hampel, 2023; Heindel et al., 2008).

Computed tomography requires projections from multiple angles, with higher angular coverage improving reconstruction quality (Pelt et al., 2018). This is typically achieved either by rotating the X-ray or γ-ray source (Shaikh et al., 2023; Bieberle et al., 2013), by employing multiple source-detector pairs (Yan et al., 2021), or by recording a single angle and reusing the same image for many angles, assuming axisymmetry (Gawandalkar and Poelma, 2024). The approach used in this paper is to employ multiple source-detector pairs, enabling simultaneous multi-angle measurements (Graas et al., 2023). This approach does not rely on an assumption of axisymmetry, whilst avoiding the complexity and restrictions in temporal resolution associated with revolving systems. In small systems with few, large bubbles it is a promising method to study time-resolved bubble-bubble interactions.

Despite its potential, simultaneous multi-angle XRT faces significant challenges in large air–water bubble columns (ID >15 cm, H/D >5), because of the long X-ray pathlength with high attenuation. This results in significant X-ray scatter and beam hardening (Heindel et al., 2008; Hubers et al., 2005).

This study investigates these limitations in a 3-angled X-ray tomography (XRT) setup, proposes correction strategies, and validates them against pressure probes, fiber probes, and literature data. With appropriate corrections, XRT achieves faster measurements and improved spatial resolution compared to fiber probes, while remaining consistent with literature data. This illustrates the potential of a 3-angled XRT setup for rapid screening of gas phase dynamics in bubble columns with complex mixtures.

2. Materials and methods

2.1. Bubble column setup

Experiments were conducted in a cylindrical bubble column with an internal diameter of 19.2 cm and an ungassed H_L of 1 m, meeting the Wilkinson scalability criteria (ID > 15 cm, H_L/ID > 5) (Wilkinson et al., 1992). Tap water was used as the liquid phase. The water was refreshed daily. The room temperature was kept constant at 19 ± 2 °C. Gas flow was controlled using a Bronkhorst mass flow controller, set to 30 L min^{-1}, 80 L min^{-1}, 100 L min^{-1} and 150 L min^{-1} (calibrated at 0 °C, 1.013 · 10^5 Pa), corresponding to mean $u_{g,s}$ of 1.81 cm s^{-1}, 4.81 cm s^{-1}, 6.01 cm s^{-1} and 9.01 cm s^{-1} over the height of the column. An overview of the setup, including the arrangement of X-ray sources and detectors, as well as the positions of pressure and fiber probes, is shown in Fig. 1. The gas sparger was a 5 mm thick perforated plate with 12 3 mm holes, resulting in an open area of 0.3 %. Further details of the sparger can be found in Appendix A: Sparger geometry.

Table 1
Distance between column center and fiber probe measurement positions and the absolute, normalized positions of fiber probe measurement. Positions were normalized by dividing by the column radius.

Position	1	2	3	4	5	6	7	8	9
Distance (cm)	7.6	5.6	3.7	1.8	−0.2	−2.0	−3.9	−5.7	−7.7
Normalized (–)	0.80	0.58	0.39	0.19	0.02	0.21	0.41	0.59	0.80

2.2. Holdup measurements

Gas holdup was quantified using three complementary techniques: pressure probes, FP, and XRT. Each method provided distinct spatial resolution and served as a basis for cross-validation.

2.2.1. Pressure probe

Global holdup in the section between 37.5 cm and 57.5 cm above the distributor (Fig. 1) was determined using gauge pressure probes (Omega PXM319-0.07G-10V). Holdup was calculated from the pressure difference according to:

$$\varepsilon_g = 1 - \frac{\Delta p}{g \cdot \rho_L \cdot \Delta H} \tag{1}$$

The pressure probes were calibrated with static liquid height at 14 and 15 different liquid heights (top and bottom probe, respectively).

2.2.2. Fiber-optic probe

Local gas holdup was measured using an optical fiber probe (A2 Photonic Sensors) (Lefebvre et al., 2022) with an acquisition frequency of 4.81 · 10^6 Hz and a measurement duration of 120 s per position. Nine radial positions were sampled (Table 1). As the data was eventually plotted over normalized radius for comparison with literature, the datapoints at position 1 & 9, 2 & 8, 3 & 7 and 4 & 6 were later combined to reduce clutter, assuming axisymmetry. The fiber was inserted from a side port at 57.5 cm height (Fig. 1). Data analysis was primarily performed using the M2 Bubble Analyzer software (A2 Photonic Sensors); for files that failed automated processing, the gas fraction was estimated by classifying signals exceeding five standard deviations above the water baseline as gas. The global gas fraction was derived from local measurements following the method from Schweitzer et al. (2001).

2.2.3. X-ray tomography

Conversion to gas fraction. Local holdup was also determined using XRT. The measurement principle for XRT relies on attenuation of the generated X-rays in the bubble column, with water having a much higher attenuation coefficient than air making it possible to distinguish the two phases. In an ideal case, the image intensity can be described by the Lambert–Beer law:

$$I_{\mathrm{meas}} = I_0 \cdot \exp\left(-\int_l \mu(l) \cdot dl\right) \tag{2}$$

where I_{meas} is the measurement image, I_0 is a reference (flatfield) image, which is the image intensity without the object of study in place, μ is the attenuation coefficient in cm^{-1} over the pathlength l in cm.

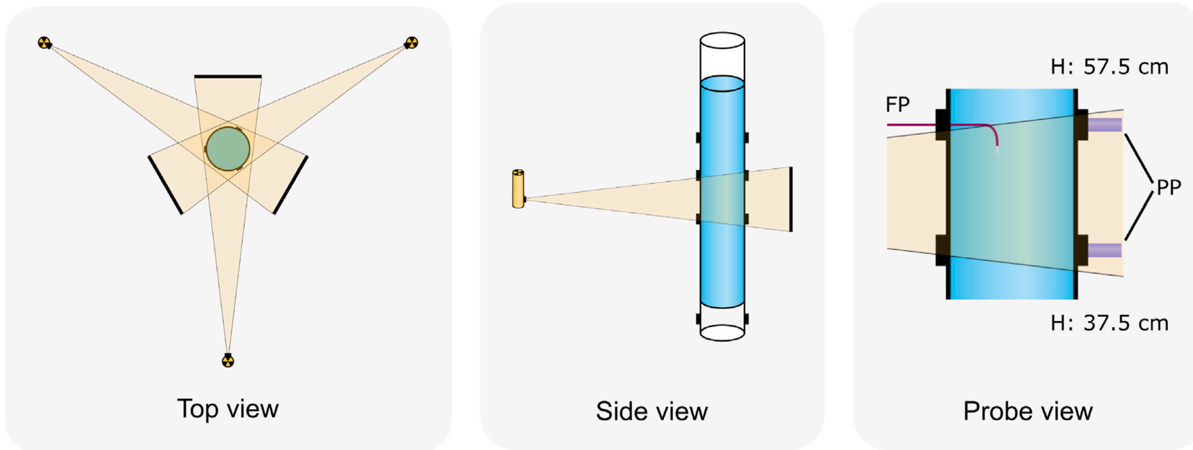

Fig. 1. Global sketch of the measurement setup with multiple X-ray sources and detectors around the column. Left: top view of the setup; Middle: side view with a single source, column and detector; Right: zoomed-in view of the pressure probes and fiber probe. FP: Fiber probe; PP: Pressure probe.

Table 2
Source amperage settings for the different voltages.

Voltage	Source	Amperage (mA)
	Source 1	0.74
120 kV	Source 2	0.78
	Source 3	0.87
	Source 1	0.58
135 kV	Source 2	0.62
	Source 3	0.69
	Source 1	0.48
150 kV	Source 2	0.50
	Source 3	0.57

In the end, we are not directly interested in the attenuation coefficient or pathlength, but in the gas fraction (ε_g) over each source-detector path. We can rewrite the Lambert–Beer equation with several reference measurements to get an expression for this:

$$\varepsilon_g = \frac{\ln(I_{\text{meas}}/I_{\text{full}})}{\ln(I_{\text{empty}}/I_{\text{full}})} \quad (3)$$

In Eq. (3) we use the image (radiographic projection) with the empty column (I_{empty}) as the reference image, and we assume a constant value for μ_{water}. The other reference used is I_{full}, an image of the column filled with ungassed water. This conversion was integrated in the tomographic algorithm. A more detailed derivation of the relation can be found in Appendix B: Gas fraction from X-ray images.

X-ray measurement setup. The experimental setup consists of three source–detector pairs positioned at 120° intervals, enabling simultaneous multi-angle acquisition. The detectors were Teledyne Dalsa Xineos 3131 detectors, measuring at full resolution (1548 × 1524 pixels) and a frequency of 22 Hz. Sources were Yxlon Y.TU 160-D06 X-ray tubes, with outgoing beams of 30° × 40°. As the required angle is roughly 12° × 12°, the beams were cropped down near the source, by placing 1 cm thick stainless steel plates in the path of the superfluous X-rays. This reduces the total outgoing radiation which in turn might reduce scatter-based noise. Source current was optimized for maximum intensity in the empty column. Source settings are summarized in Table 2. The relative source-detector positions and tilts were determined through the method developed by Graas et al. (2023), with some small updates. A personal fork of the code used for this (the CaTE package - https://github.com/adriaangraas/CaTE) can be found at (https://github.com/RikVolger/CaTE/tree/develop). The exact, static, version of the code can be found at https://github.com/RikVolger/CaTE/releases/tag/three-angle-tomography_v1. The found geometry was then corrected for minor offsets in the actual column position within the source-detector setup through an optimization step on the basis of pathlength-dependent intensity profiles. Details can be found in Appendix C: Pathlength based geometry optimization, the implementation can be found in the file `optimize_geometry.py` in https://github.com/RikVolger/3ct-tools/releases/tag/v1.0-3at-rev1. Code for further analysis and creating all figures in this paper can be found at https://github.com/RikVolger/practical-3-angle-tomography/releases/tag/v1.0-rev1.

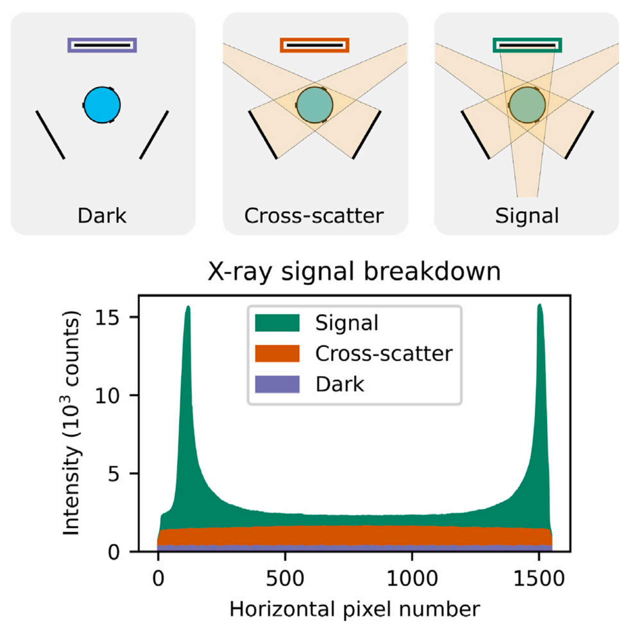

Fig. 2. Breakdown of the xray signal into dark (background noise), cross-scatter (Xray from unassociated sources) and measurement signal. Values from a horizontal line at vertical pixel number 1000 on detector 2.

Signal breakdown. An analysis of the recorded detector signal (Fig. 2) identifies multiple sources of noise. When no sources were active, there was a noteworthy and consistent dark signal picked up by the detectors. With the sources active, a much more pronounced contribution comes from each detector picking up scattered X-rays from the other sources, which further increases the baseline signal. The Lambert–Beer equation (Eq. (2)) dictates that the intensity approaches 0 for infinite pathlengths, which should be reflected in the data to justify the processing approach. The offsets due to the dark image and

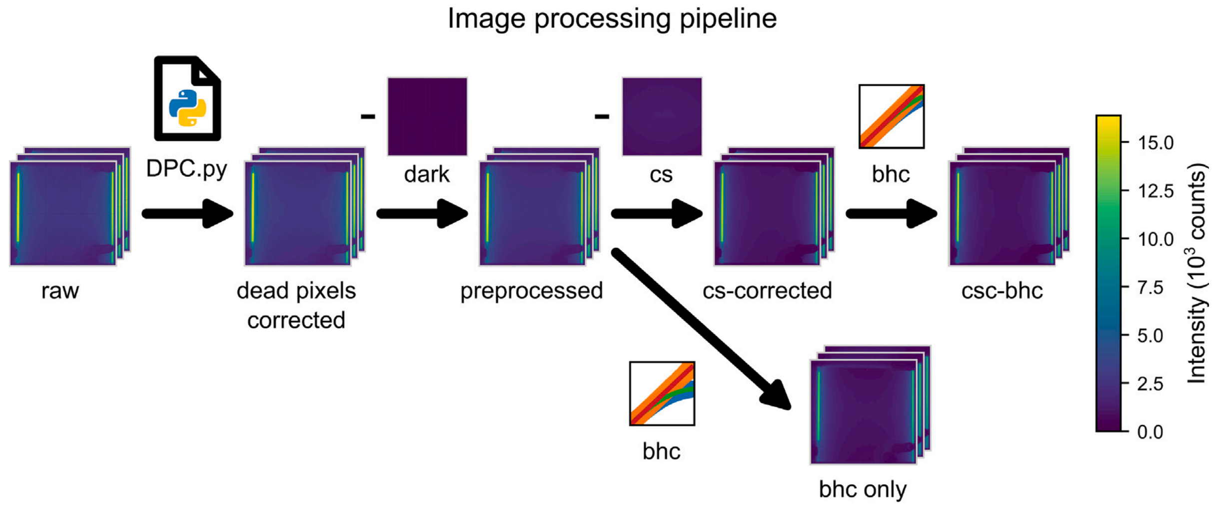

Fig. 3. Visualization of the processing pipeline to the different corrected image files. Dead pixel lines are identified and corrected for through horizontal/vertical interpolation. Dark image is subtracted, in the top series followed by subtraction of cross-scatter (cs) and finally a correction for the remaining pathlength-dependency of μ (bhc). In the bottom branch, bhc is applied directly to the preprocessed image. DPC: Dead Pixel Correction, cs: cross-scatter, bhc: beam hardening correction, csc-bhc: cross-scatter corrected and beam hardening corrected.

cross-scatter mean that this requirement is not met, and a number of processing steps are needed to obtain useful data from the setup. The overall processing pipeline is illustrated in Fig. 3. For all images, the processing started with a correction of dead pixel lines by horizontal and vertical interpolation of the neighbors, followed by subtraction of the dark signal.

Cross-scatter correction. Cross-scatter noise from X-rays between sources and non-corresponding detectors was characterized by activating two sources and measuring the third detector (Fig. 2). The per-pixel mean intensity of this signal was subtracted from the pre-processed image (Fig. 3). As cross-scatter is the result of beam attenuation, it was expected that it would be dependent on the global gas fraction with higher gas fractions leading to less cross-scatter. This relation was explored and reported in Appendix E: Cross-Scatter characterization but found to be rather weak which justifies the subtraction of a constant mean.

Beam hardening correction. When broad-spectrum X-rays are attenuated, the different energy photons are attenuated at different rates, with low-energy photons being attenuated more than high-energy photons. This leads to a reduction of the effective attenuation over longer paths, invalidating the assumption of a constant μ_{water} - a phenomenon called beam hardening (Alles and Mudde, 2007; Heindel et al., 2008). Beam hardening was detected by plotting $-\ln(I_{\text{full}}/I_{\text{empty}})$ against pathlength (l) through the column with ungassed water (Fig. 4, blue circles). For a constant μ_{water}, the raw data should fall on a straight line:

$$I_{\text{full}} = I_{\text{empty}} \cdot e^{(-\mu_{water} \cdot l)} \tag{4}$$

$$-\ln \frac{I_{\text{full}}}{I_{\text{empty}}} = \mu_{water} \cdot l \tag{5}$$

Instead, the raw data curves off after 10 cm, indicating a pathlength-dependency of the attenuation, likely due to beam hardening.

The approach chosen was to correct the image data to reflect a constant μ_{water} by remapping the recorded data, largely inspired by Hubers et al. (2005). For this purpose, first the relation between $-\ln I_{\text{full}}/I_{\text{empty}}$ and pathlength l was fit with a third order polynomial:

$$-\ln \frac{I_{\text{full}}}{I_{\text{empty}}} = x_1 \cdot l^3 + x_2 \cdot l^2 + x_3 \cdot l + x_4 \tag{6}$$

The linear attenuation μ_{water} was calculated from the first 3 cm of pathlength and combined with the offset of the polynomial (x_4) to obtain

$$-\ln \frac{I_{\text{cor}}}{I_{\text{empty}}} = \mu_{water} + x_4 \tag{7}$$

$$I_{\text{cor}} = I_{\text{empty}} \cdot e^{(-\mu_{water} \cdot l - x_4)} \tag{8}$$

For each measurement image (I_{meas}), the value of $-\ln I_{\text{meas}}/I_{\text{empty}}$ was interpolated in the polynomial (Eq. (6)) to find the corresponding pathlength l. This pathlength was then used in Eq. (8) to obtain the beam hardening corrected image (I_{cor}), fitting a linear attenuation profile (Corrected data in Fig. 4). The same was done for each I_{full} and I_{empty}.

Details on the calculation of pathlengths can be found in Appendix D: Pathlength calculations.

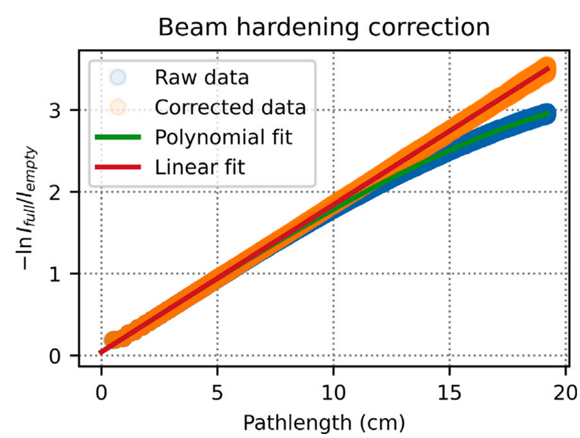

Fig. 4. Beam hardening correction visualized with cross-scatter corrected data. The raw data is fit to a third-order polynomial (Polynomial fit), and then projected on a linear relation based on the attenuation in the first 3 cm of material (Linear fit) resulting in the corrected data.

Tomography. Tomography was performed using the ASTRA Toolbox (van Aarle et al., 2016, 2015; Palenstijn et al., 2011) with some setup-specific changes based on Graas et al. (2023). The specific implementation can be found on GitHub (https://github.com/RikVolger/fluidized-bed-ct/releases/tag/v1.0-3at-rev1) and in the supporting data (https://doi.org/10.4121/29b1c43a-7c80-4fc4-a651-6e0e710b77ae).

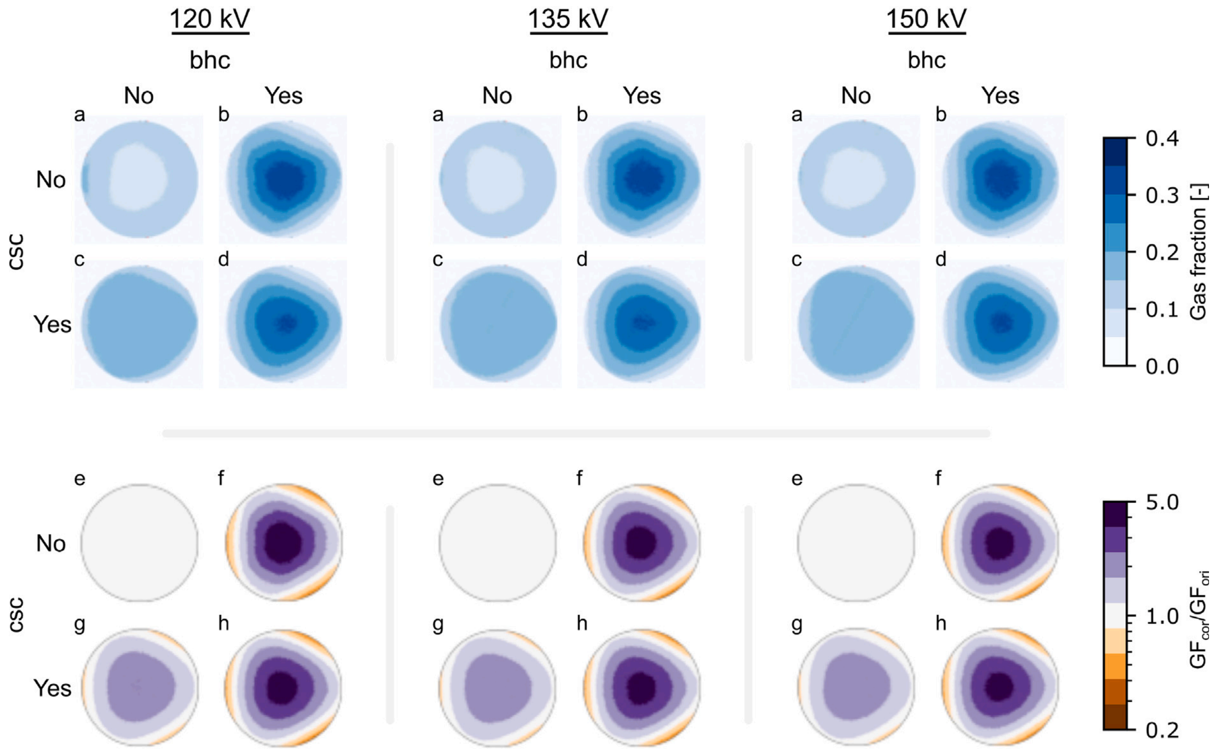

Fig. 5. Comparison of the effect of different corrections on the holdup profile at different tube voltage settings, all at a $u_{g,s}$ of 8.63 cm s^{-1}. The top series present the gas fractions (GF) obtained from reconstruction of uncorrected and corrected images, where *a* is reconstructed on the basis of the preprocessed image, *b* on the basis of the bhc-only image, *c* with the cs-corrected image and *d* with the csc-bhc image. Gas fractions are averaged over the height of the reconstruction. The bottom series show the result of dividing the gas fractions obtained with the different corrections (GF_{cor}) by the gas fraction in the uncorrected case (GF_{ori}) at the same voltage, giving an indication of effect size of each correction. csc: Cross-Scatter Corrected, bhc: Beam Hardening Corrected.

The reconstruction volume was a box with sides of 21 cm and a height of 15 cm. The voxels were cubes with 0.1 cm sides leading to a reconstruction box of 210 × 210 × 150 voxels. The reconstruction volume was initialized with all zeros. Reconstruction was limited to a cylindrical mask with a diameter of 19.2 cm (ID of the column). The `SIRT3D-CUDA` method was used for reconstructing on an NVIDIA GeForce RTX 3090 GPU with 24 GB VRAM. Reconstruction values were constrained between 0.0 and 1.0, as these are the physical limits for gas fraction. Reconstructions were run for 20 iterations to avoid overfitting to noise.

The effects of the data correction steps were investigated by applying the same reconstruction algorithm to four different base images: preprocessed, cross-scatter corrected (csc), beam hardening corrected (bhc) and cross-scatter and beam hardening corrected (csc-bhc) (Fig. 3). These images were used to calculate 'holdup images' through Eq. (3), which were then time-averaged and used as input for the tomography steps.

Radial profiles and global holdup. Radial holdup profiles for the radial holdup plots were obtained by averaging voxels at equal radii (assuming axisymmetry), while global holdup for the global holdup plot was calculated per horizontal slice, reporting mean and standard deviation over 40 slices (4 cm).

3. Results & discussion

Two major sources of measurement error in the XRT setup were identified: cross-scatter and beam hardening. Correction strategies for each were implemented and evaluated individually and in combination. Beam hardening is expected to diminish at higher tube voltages due to the relative abundance of higher-energy photons in the X-ray spectrum (Alles and Mudde, 2007; Kyriakou et al., 2010; Hofmann et al., 2022). To investigate this effect, measurements at three different voltage settings with the different corrections were compared (Fig. 5). In the top series (a–d), the gas fractions for the different corrections are reported for all three voltages. In the bottom series (e–h), the comparison between the corrected gas fraction and original, uncorrected, gas fraction is shown as a fold-change. The expected result is that the beam hardening correction has less impact at higher voltages. Following that, the intensity in the fold-change due to the beam hardening correction should be lower at higher voltages.

The data requires significant correction to obtain sensible gas fractions. The expected radial gas holdup profile in a bubble column in the heterogeneous regime is parabolic, with a maximum in the center and near-zero holdup at the walls (Schweitzer et al., 2001; Besagni, 2021; Kumar et al., 1997). The uncorrected profiles (Fig. 5a) exhibit the opposite of this behavior, confirming the necessity of corrections even at the highest voltages possible in our setup (150 kV). Applying only the cross-scatter correction (Fig. 5c) resulted in fairly uniform holdup across the column cross-section, whereas applying only the beam hardening correction (Fig. 5b) produced the expected sharper, parabolic-like profile. Combining both corrections (Fig. 5d) yielded slightly lower holdup values but a similar profile. The obtained cross-sectional holdup profiles resemble a rounded triangle, an artefact from using only 3 angles (Graas et al., 2023). In tomographic reconstructions with only 3 angles, the ideal reconstruction of a circular object like the bubble column under study here is a triangle. For the column we suppress this by imposing a circular mask to the reconstruction volume, but this cannot be done for the gas inside the column without imposing an assumption of axisymmetry. Therefore, the variations inside the column are solved to a roughly triangular shape. The bottom panels (e-h) in Fig. 5 illustrate the relative effect of the corrections compared to uncorrected (Fig. 5e) images. Contrary to our initial expectations, all three combinations of corrections (csc (Fig. 5g), bhc (Fig. 5f) and csc-bhc (Fig. 5h)) are roughly similar across the different tube voltage settings.

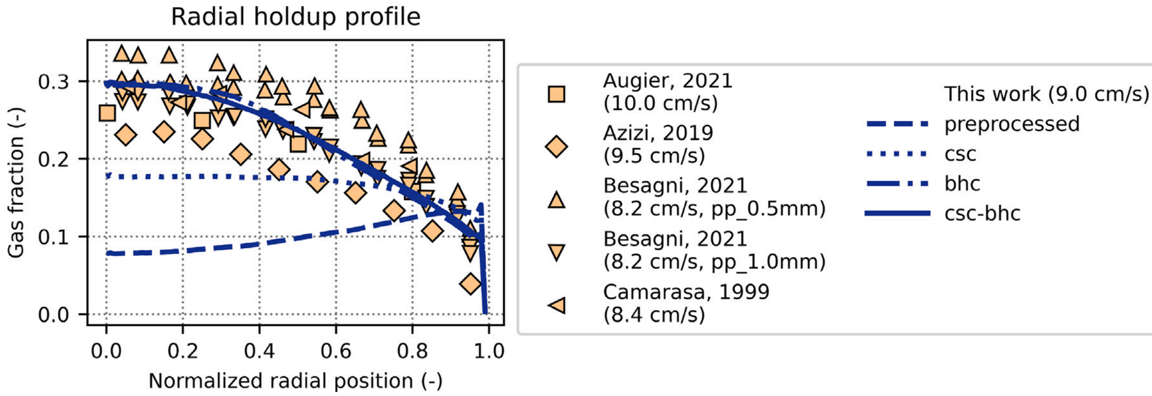

Fig. 6. Effect of different corrections on the radial holdup profile, compared to literature. Data from Azizi et al. (2019), Besagni (2021), Camarasa et al. (1999), Wu et al. (2001), Kumar et al. (1997). Besagni (2021) obtained separate data with perforated plates with 0.5 mm and 1.0 mm holes, which are both included here. All current results correspond to the 150 kV series.

The similarity between bhc and csc-bhc shows that the beam hardening correction procedure also corrects for scatter effects and functions as a more general correction method. The profiles from the different tube settings and corrections are further visualized in Appendix F. A comparison of all different corrections at all different $u_{g,s}$ can also be found there. These figures reinforce the observation that an increase in voltage does not improve the reconstructions, but do not provide further noteworthy new insights. The similarity between 135 kV and 150 kV shows that beam hardening cannot be mitigated through voltage increase within the operating window of the equipment. The software-based post processing corrections presented here are adequate to mitigate the impact and further quantitative comparisons supporting this approach are presented below. If one wants to reduce beam hardening to start with, a hardware-based alternative would be to filter the outgoing X-rays with a thin slice of metal, pre-hardening the beam.

3.1. Corrections vs. literature

The dataset with a $u_{g,s}$ of 8.6 cm s^{-1} measured at 150 kV was chosen for detailed analysis of the corrections and compared to literature profiles (Fig. 6). The uncorrected data (preprocessed) showed no resemblance to literature trends. Cross-scatter correction alone (csc) improved agreement in magnitude at the edges but failed to reproduce the expected curvature, not reaching the gas fractions of 0.2 to 0.35 in the center of the column as found in literature. Reconstruction with bhc images produced profiles closely matching those reported by Besagni (2021), Camarasa et al. (1999) and Kumar et al. (1997). The use of csc-bhc yields a similar shape to bhc alone, but with slightly higher gas fraction values at the edges and slightly lower values in the center. The biggest difference between the two is located at a normalized radius of 0.3, where the gas fraction from the combined correction is roughly 5 % lower than that from beam hardening alone. Both the combined correction and beam hardening correction alone fall well within literature ranges, resulting in no clear 'best' method. Some literature discrepancies are noteworthy: the low values from Azizi et al. (2019) could stem from either the small column diameter (10 cm) or from the use of highly purified water leading to increased bubble coalescence (Kumar et al., 1997). Wu et al. (2001) reported exceptionally high holdup values, especially towards the column walls, while using a similar sparger to Besagni (2021). It is worth noting that Azizi et al. (2017), Kumar et al. (1997), Wu et al. (2001) used tomography methods, while Besagni (2021), Camarasa et al. (1999) used optical fiber probe techniques. It is important to note that the sharp decrease of gas fraction close to the wall in our data is not resolved, but an artefact of the column mask used in reconstruction, which forces the last value at the column radius to 0.

3.2. Literature agreement at different $u_{g,s}$

The fully corrected gas fraction data at different $u_{g,s}$ was compared to literature data at similar $u_{g,s}$ and was found to agree well across the board (Fig. 7). A notable discrepancy is between our data at 4.7 cm s^{-1} and the fiber probe data by Esmaeili et al. (2015), but this might be due to the low H_L/ID ratio of 3 in their work resulting in deviations in gas fraction. At the lower $u_{g,s}$ we obtained a somewhat sharper profile than comparable literature works, but this seems to be within the margin of error. The same analysis was also performed with the bhc-only data (Appendix G: BHC-Only Radial profile), resulting in similar profiles. From these comparisons of outcomes alone, it is not possible to pick a better method between the csc-bhc and bhc corrections.

3.3. XRT vs fiber probes

The XRT results were also compared with our own FP measurements obtained under identical conditions (Fig. 8) where profile shapes were always in good agreement, but magnitude exhibited notable discrepancies between the methods. At low $u_{g,s}$ (1.73 cm s^{-1}), the profiles match closely, although the XRT profile is consistently slighly higher. With increasing $u_{g,s}$, the XRT-based gas fractions rise significantly faster than the FP results. Considering the good agreement of XRT with literature profiles found in Fig. 7, this implies that the fiber probe underestimates holdup at higher $u_{g,s}$. This could be due to the chaotic flow pattern resulting in more downflowing bubbles, which are not picked up well with a down-facing fiber probe. Another (complementary) explanation is the presence of small bubbles that may not be consistently punctured by the probe tip.

The XRT method is significantly more time-efficient at measuring holdup profiles. Obtaining a single 9-point gas holdup profile from FP measurements took 25 min, while the XRT measurement producing a near-continuous profile took 2 min to obtain through the bhc method, or 9 min through the csc-bhc method due to the required scatter measurements. While the csc-bhc method provides more theoretical insight into the measurement characteristics, the bhc method is clearly preferred from an efficiency point of view.

3.4. Global holdup profile

The global gas fraction values derived from XRT, FP, and pressure probe (PP) were compared to literature data, showing good overall agreement (Fig. 9). The XRT results with bhc and csc-bhc are difficult to distinguish in the plot, as they obtain nearly the same results. They both reproduced global gas fractions at the high end of literature values for most superficial gas velocities. The fiber probe data agrees well with the PP data, both being at the low end of literature values. The slight

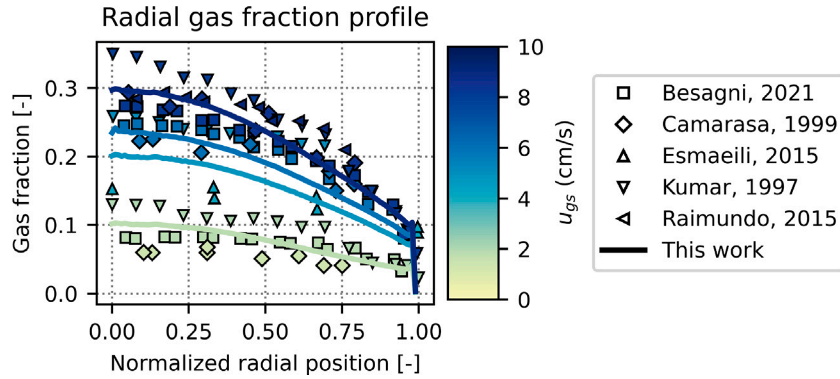

Fig. 7. Comparison of the radial gas fraction profile between csc-bhc XRT results at 150 kV and literature data at comparable superficial gas velocities. Data from Besagni (2021), Camarasa et al. (1999), Esmaeili et al. (2015), Kumar et al. (1997), Raimundo (2015). Here, only the results with the 1 mm sparger holes from Besagni (2021) were used. Markers are literature values and lines are measurements from this work, with marker and line colors indicating their superficial gas velocity ($u_{g,s}$).

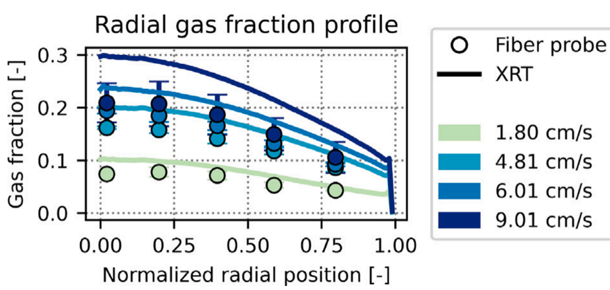

Fig. 8. Comparison between X-ray tomography results and optical fiber probe measurements at different superficial gas velocities.

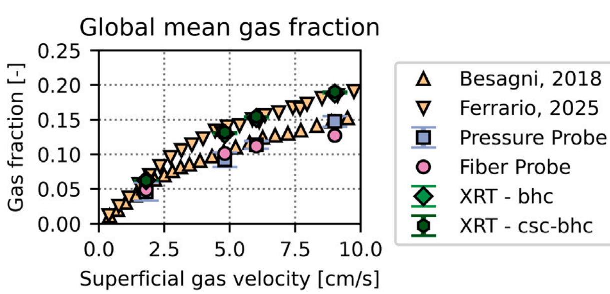

Fig. 9. Comparison between global holdup measurements based on XRT, fiber probe (FP), pressure probe (PP), and literature values (Ferrario et al., 2025; Besagni et al., 2018). From Besagni et al. (2018), the data with the spider sparger was used.

underestimation by the fiber probes was expected from Fig. 8, while the results from differential pressure measurement were expected to provide spatially unresolved but reliable fallback values. The agreement of the PP with the fiber probe data implies that while the radial profiles from XRT measurements agree well with literature values for similar setups, they might overpredict the holdup in our specific setup. This could be further remediated by scaling the obtained XRT profiles with a constant, such that the global mean gas fraction from XRT perfectly matches the PP data. The need for such an extra correction term is an indication that a source of measurement error remains in the XRT method, even after cross-scatter and/or beam hardening corrections. The nature of this source is not clear to us at the moment.

Considering the variability between Besagni et al. (2018) and Ferrario et al. (2025), which were both performed with the liquid bed expansion technique in the same lab with a very similar bubble column setup, the variability between methods in our work is not unexpected.

4. Conclusion

This work validates a three-angled XRT setup for measuring local gas fraction in bubble columns. Experiments were performed in a column with H_L/ID > 5 and an ID exceeding 15 cm, ensuring scalable hydrodynamic conditions representative of industrially relevant systems. The results demonstrate that the proposed configuration is suitable for obtaining radial gas fraction profiles in large-diameter columns.

Accurate tomographic reconstruction requires correction of deviations from the Lambert–Beer law caused by detector artefacts (dark signal), X-ray scattering and beam hardening of the polychromatic X-rays. The dark signal offset could easily be corrected for with few extra measurements. Cross-scatter and beam hardening effects could adequately be addressed sequentially, but the beam hardening correction procedure alone was found to also compensate for scatter-related deviations. With this correction in place, the reconstructed gas fraction profiles exhibit the expected parabolic profile. These profiles also quantitatively match literature data over a range of superficial gas velocities.

When both methods are available, XRT is the preferable method over fiber probe measurements because of the combination of higher accuracy and shorter measurement times. Fiber probes likely underestimate gas fraction at higher $u_{g,s}$, possibly due to their preferred sampling of upflowing bubbles, while XRT maintain accuracy over $u_{g,s}$. However, the spatial resolution of XRT is insufficient to characterize individual bubbles, so for quantification of the bubble size- and speed distributions necessary to draw conclusions on interfacial area and mass transfer characteristics, FP remains essential in opaque flows.

Overall, XRT enables rapid and reliable acquisition of gas fraction profiles with a factor twelve reduction in measurement time compared to fiber probe techniques. This makes XRT attractive for systematic studies of the effects of superficial gas velocity and fluid composition on gas distribution in bubble columns. Additionally, the temporal resolution of XRT may allow to resolve temporal dynamics in the macroscopic flow, e.g. plume oscillations. Further research is required to explore this possibility given the substantial tangential artefacts introduced in the low-angle tomographic reconstructions. A fallback for comparisons between CFD simulations and X-ray data would be comparison of the 2D transmission images with forward projections from the CFD data.

Looking ahead, this methodology could be applied to systems containing dissolved solutes or biomass, to address coalescence inhibition and complex multiphase interactions. Furthermore, coupling XRT-based holdup measurements with volume-specific mass transfer coefficient ($k_L a$) measurement would create valuable datasets for refining design correlations and validating advanced CFD models.

Acronyms

bhc beam hardening corrected
BSD bubble size distribution
CFD computational fluid dynamics
csc cross-scatter corrected
csc-bhc cross-scatter and beam hardening corrected
FP fiber probe
ID inner diameter
PP pressure probe
XRT X-ray tomography

CRediT authorship contribution statement

Rik Volger: Writing – review & editing, Writing – original draft, Visualization, Software, Methodology, Investigation, Formal analysis, Data curation, Conceptualization. **Sam J. den Hartog:** Writing – review & editing, Software, Methodology. **Evert C. Wagner:** Writing – review & editing, Resources, Methodology, Conceptualization. **Cees Haringa:** Writing – review & editing, Supervision, Project administration, Conceptualization.

Declaration of competing interest

The authors declare that they have no known competing financial interests or personal relationships that could have appeared to influence the work reported in this paper.

Appendix A. Supplementary data

Supplementary material related to this article can be found online at https://doi.org/10.1016/j.ijmultiphaseflow.2026.105873.

Data availability

Data and code have been uploaded to 4TU.ResearchData repository: https://doi.org/10.4121/29b1c43a-7c80-4fc4-a651-6e0e710b77ae.

References

Alles, J., Mudde, R.F., 2007. Beam hardening: analytical considerations of the effective attenuation coefficient of x-Ray tomography. Med. Phys. 34 (7), 2882–2889.
Augier, F., Raimundo, P.M., 2021. Effect of Rheology on mass transfer and bubble sizes in a bubble column operated in the heterogeneous regime. Can. J. Chem. Eng. 99 (5), 1177–1185.
Azizi, S., Yadav, A., Lau, Y.M., Hampel, U., Roy, S., Schubert, M., 2017. On the experimental investigation of gas-liquid flow in bubble columns using ultrafast X-ray tomography and radioactive particle tracking. Chem. Eng. Sci. 170, 320–331.
Azizi, S., Yadav, A., Lau, Y.M., Hampel, U., Roy, S., Schubert, M., 2019. Hydrodynamic correlations for bubble columns from complementary UXCT and RPT measurements in identical geometries and conditions. Chem. Eng. Sci. 208, 115099.
Becker, S., De Bie, H., Sweeney, J., 1999. Dynamic flow behaviour in bubble columns. Chem. Eng. Sci. 54 (21), 4929–4935.
Besagni, G., 2021. Bubble column fluid dynamics: A novel perspective for flow regimes and comprehensive experimental investigations. Int. J. Multiph. Flow 135, 103510.
Besagni, G., Gallazzini, L., Inzoli, F., 2018. Effect of gas sparger design on bubble column hydrodynamics using pure and binary liquid phases. Chem. Eng. Sci. 176, 116–126.
Besagni, G., Inzoli, F., 2016. Comprehensive experimental investigation of counter-current bubble column hydrodynamics: holdup, flow regime transition, bubble size distributions and local flow properties. Chem. Eng. Sci. 146, 259–290.
Bieberle, A., Härting, H.-U., Rabha, S., Schubert, M., Hampel, U., 2013. Gamma-ray computed tomography for imaging of multiphase flows. Chem. Ing. Tech. 85 (7), 1002–1011.
Camarasa, E., Vial, C., Poncin, S., Wild, G., Midoux, N., Bouillard, J., 1999. Influence of coalescence behaviour of the liquid and of gas sparging on hydrodynamics and bubble characteristics in a bubble column. Chem. Eng. Process.: Process. Intensif. 38 (4–6), 329–344.
Chisti, M.Y., Moo-Young, M., 1987. Airlift reactors: Characteristics, applications and design considerations. Chem. Eng. Commun. 60 (1–6), 195–242.
Draw, M., Rzehak, R., 2024. Euler-Euler simulation of a bubble column flow up to high gas fraction. Int. J. Multiph. Flow 181, 104969.
Esmaeili, A., Guy, C., Chaouki, J., 2015. The effects of liquid phase rheology on the hydrodynamics of a gas–liquid bubble column reactor. Chem. Eng. Sci. 129, 193–207.
Ferrario, A., Varallo, N., Besagni, G., Mereu, R., 2025. Influence of the gas phase on a large-scale bubble column fluid dynamics: gas holdup, flow regime transitions, and bubble size distributions. Chem. Eng. Sci. 302, 120792.
Gawandalkar, U.U., Poelma, C., 2024. The characteristics of bubbly shock waves in a cavitating axisymmetric venturi via time-resolved X-ray densitometry. J. Fluid Mech. 988, A34.
Graas, A.B.M., Wagner, E.C., van Leeuwen, T., van Ommen, J.R., Batenburg, K.J., Lucka, F., Portela, L.M., 2023. X-Ray tomography for fully-3D time-resolved reconstruction of bubbling fluidized beds. Powder Technol. 119269.
Hampel, U., 2023. Multiphase imaging techniques. In: Handbook of Multiphase Flow Science and Technology. Springer, pp. 591–624. http://dx.doi.org/10.1007/978-981-287-092-6_14.
Heindel, T.J., 2011. A review of X-Ray flow visualization with applications to multiphase flows. J. Fluids Eng. 133 (074001).
Heindel, T.J., Gray, J.N., Jensen, T.C., 2008. An X-ray system for visualizing fluid flows. Flow Meas. Instrum. 19 (2), 67–78.
Helchi, S., Emamshoushtari, M.M., Pajoum Shariati, F., Bonakdarpour, B., Haddadi, B., 2024. Data-driven gas holdup correlation in bubble column reactors considering alcohol concentration and carbon number. ChemEngineering 8 (6), 117.
Hofmann, J., Flisch, A., Zboray, R., 2022. Principles for an implementation of a complete CT reconstruction tool chain for arbitrary sized data sets and its GPU optimization. J. Imaging 8 (1), 12.
Hubers, J.L., Striegel, A.C., Heindel, T.J., Gray, J.N., Jensen, T.C., 2005. X-Ray computed tomography in large bubble columns. Chem. Eng. Sci. 60 (22), 6124–6133.
Kumar, S.B., Moslemian, D., Duduković, M.P., 1997. Gas-holdup measurements in bubble columns using computed tomography. AIChE J. 43 (6), 1414–1425.
Kyriakou, Y., Meyer, E., Prell, D., Kachelrieß, M., 2010. Empirical beam hardening correction (EBHC) for CT. Med. Phys. 37 (10), 5179–5187.
Lefebvre, A., Mezui, Y., Obligado, M., Gluck, S., Cartellier, A., 2022. A new, optimized Doppler optical probe for phase detection, bubble velocity and size measurements: investigation of a bubble column operated in the heterogeneous regime. Chem. Eng. Sci. 250, 117359.
Mcclure, D.D., Norris, H., Kavanagh, J.M., Fletcher, D.F., Barton, G.W., 2014. Validation of a computationally efficient computational fluid dynamics (CFD) model for industrial bubble column bioreactors.
Nedeltchev, S., Marchini, S., Schubert, M., Hampel, U., 2024. New approaches for prediction of flow regime boundaries and overall gas holdups in a bubble column operated with aqueous solutions of 2-pentanol. J. Chem. Eng. Jpn. 57 (1), 2330388.
Palenstijn, W.J., Batenburg, K.J., Sijbers, J., 2011. Performance improvements for iterative electron tomography reconstruction using graphics processing units (GPUs). J. Struct. Biol. 176 (2), 250–253.
Pelt, D., Batenburg, K., Sethian, J., 2018. Improving tomographic reconstruction from limited data using mixed-scale dense convolutional neural networks. J. Imaging 4 (11), 128.
Poelma, C., 2020. Measurement in opaque flows: A review of measurement techniques for dispersed multiphase flows. Acta Mech. 231 (6), 2089–2111.
Prasser, H.M., Scholz, D., Zippe, C., 2001. Bubble size measurement using wire-mesh sensors. Flow Meas. Instrum. 12 (4), 299–312.
Puiman, L., Abrahamson, B., van der Lans, R.G., Haringa, C., Noorman, H.J., Picioreanu, C., 2022a. Alleviating mass transfer limitations in industrial external-loop syngas-to-ethanol fermentation. Chem. Eng. Sci. 259, 117770.
Puiman, L., Elisiário, M.P., Crasborn, L.M., Wagenaar, L.E., Straathof, A.J., Haringa, C., 2022b. Gas mass transfer in syngas fermentation broths is enhanced by ethanol. Biochem. Eng. J. 108505.
Raimundo, P.M., 2015. Analysis and Modelization of Local Hydrodynamics in Bubble Columns (Ph.D. thesis). Université Grenoble Alpes.
Sanyal, J., Vásquez, S., Roy, S., Dudukovic, M.P., 1999. Numerical simulation of gas–liquid dynamics in cylindrical bubble column reactors. Chem. Eng. Sci. 54 (21), 5071–5083.
Schweitzer, J.-M., Bayle, J., Gauthier, T., 2001. Local gas hold-up measurements in fluidized bed and slurry bubble column. Chem. Eng. Sci. 56 (3), 1103–1110.
Shaikh, A., Taha, M.M., Al-Dahhan, M.H., 2023. Phases distribution in slurry bubble columns: insights from single-source computed tomography and gas holdup measurements. Flow Meas. Instrum. 93, 102441.
van Aarle, W., Palenstijn, W.J., Cant, J., Janssens, E., Bleichrodt, F., Dabravolski, A., Beenhouwer, J.D., Batenburg, K.J., Sijbers, J., 2016. Fast and flexible X-ray tomography using the ASTRA toolbox. Opt. Express 24 (22), 25129–25147.
van Aarle, W., Palenstijn, W.J., De Beenhouwer, J., Altantzis, T., Bals, S., Batenburg, K.J., Sijbers, J., 2015. The ASTRA toolbox: A platform for advanced algorithm development in electron tomography. Ultramicroscopy 157, 35–47.
van 't Riet, K., 1983. Mass transfer in fermentation. Trends Biotechnol. 1 (4), 113–119.
Villafañe, L., Aliseda, A., Ceccio, S., Di Marco, P., Machicoane, N., Heindel, T.J., 2025. 50 years of international journal of multiphase flow: experimental methods for dispersed multiphase flows. Int. J. Multiph. Flow 189, 105239.

Volger, R., Puiman, L., Haringa, C., 2024. Bubbles and broth: A review on the impact of broth composition on bubble column bioreactor hydrodynamics. Biochem. Eng. J. 201, 109124.
Wang, Y., Shen, X., Zhang, H., Wang, T., 2024. Marangoni effect on hydrodynamics and mass transfer behavior in an internal loop airlift reactor under elevated pressure. AIChE J. 70 (2), e18291.
Wilkinson, P.M., Spek, A.P., van Dierendonck, L.L., 1992. Design parameters estimation for scale-up of high-pressure bubble columns. AIChE J. 38 (4), 544–554.
Wu, Y., Cheng Ong, B., Al-Dahhan, M.H., 2001. Predictions of radial gas holdup profiles in bubble column reactors. Chem. Eng. Sci. 56 (3), 1207–1210.
Yan, M., Ma, B., Tian, B., Hu, G., Wu, R., Wang, S., 2021. Design, simulation and reconstruction for a fast speed two-phase flow CT with 241Am Gamma ray sources. Ann. Nucl. Energy 151, 107970.